Nucl Eng Technol 47 (2015) 523–533

Available online at www.sciencedirect.com

ScienceDirect

journal homepage: http://www.journals.elsevier.com/nuclear-engineering-and-technology/

Invited Article

THREE-DIMENSIONAL FLOW PHENOMENA IN A WIRE-WRAPPED 37-PIN FUEL BUNDLE FOR SFR

JAE-HO JEONG[*], *JIN YOO*, *KWI-LIM LEE*, *and KWI-SEOK HA*

Korea Atomic Energy Research Institute, 989-111 Daedeok-daero, Yuseoung-gu, Daejeon, 305-353, Republic of Korea

ARTICLE INFO

Article history:
Received 25 February 2015
Received in revised form
31 May 2015
Accepted 2 June 2015
Available online 14 June 2015

Keywords:
Computational fluid dynamics
Reynolds-averaged Navier-Stokes
Vortex
Wire spacer

ABSTRACT

Three-dimensional flow phenomena in a wire-wrapped 37-pin fuel assembly mock-up of a Japanese loop-type sodium-cooled fast reactor, Monju, were investigated with a numerical analysis using a general-purpose commercial computational fluid dynamics code, CFX. Complicated and vortical flow phenomena in the wire-wrapped 37-pin fuel assembly were captured by a Reynolds-averaged Navier–Stokes flow simulation using a shear stress transport turbulence model. The main purpose of the current study is to understand the three-dimensional complex flow phenomena in a wire-wrapped fuel assembly to support the license issue for the core design. Computational fluid dynamics results show good agreement with friction factor correlation models. The secondary flow in the corner and edge subchannels is much stronger than that in an interior subchannel. The axial velocity averaged in the corner and edge subchannels is higher than that averaged in the interior subchannels. Three-dimensional multiscale vortex structures start to be formed by an interaction between secondary flows around each wire-wrapped pin. Behavior of the large-scale vortex structures in the corner and edge subchannels is closely related to the relative position between the hexagonal duct wall and the helically wrapped wire spacer. The small-scale vortex is axially developed in the interior subchannels. Furthermore, a driving force on each wire spacer surface is closely related to the relative position between the hexagonal duct wall and the wire spacer.

1. Introduction

The sodium-cooled fast reactor (SFR) system is one of the nuclear reactors in which recycling of transuranics, by reusing spent nuclear fuels, sustains the fission chain reaction. This feature strongly motivated the Korea Atomic Energy Research Institute, Daejeon, Korea to start a prototype Gen-IV sodium-cooled fast reactor design project under the national nuclear R&D program. Generally, the SFR system has a tight fuel bundle package and high power density. Sodium has higher

* *Corresponding author.*
E-mail address: jhjeong@kaeri.re.kr (J.-H. Jeong).

http://dx.doi.org/10.1016/j.net.2015.06.001
1738-5733/Copyright © 2015, Published by Elsevier Korea LLC on behalf of Korean Nuclear Society.

thermal conductivity and a higher boiling temperature than water. This can make the core design more compact than light water reactors through the use of narrower sub-channels. The fuel assembly of the SFR system consists of long and thin wire-wrapped fuel bundles arranged in a triangular array in a hexagonal duct. The main purpose of a wire spacer is to avoid collisions between adjacent rods. Furthermore, vortex-induced vibration can be mitigated by wire spacers and the secondary flow, due to helical-type wire spacers, can enhance convective heat transfer.

Many experimental studies have been conducted to understand the thermal-hydraulics of wire-wrapped fuel bundles. Novendstern [1] developed a semiempirical model that can predict the pressure loss of a turbulent region in a hexagonal array of rods with a wire spacer. Rehme [2] introduced an effective method to consider the number of wire-wrapped bundles. Engel et al. [3] proposed an intermittency factor to calculate the friction factor in transition flow. Cheng and Todreas [4] introduced their friction factor correlation and mixing geometry that are calibrated by the available world data. Roidt et al. [5] discussed experimental results in detail: static pressure gradients and detailed axial velocity mapping in inboard and peripheral channels. Chun and Seo [6] performed a comparative study of five existing correlations and identified the best performing correlations in a sub-channel pressure drop analysis. Choi et al. [7] measured the pressure drop in a 271-pin-fuel assembly of a liquid metal reactor and compared the results with the existing correlations.

Most numerical studies that have been conducted in the nuclear fields have been based on simplified sub-channel analysis codes such as COBRA [8], SABRE [9], ASFRE [10], and MATRA-LMR [11]. The subchannel analysis codes calculate the temperature, pressure, and velocity values averaged in a sub-channel, which comprise the full mixed state of flow fields in a sub-channel. The subchannel analysis approach was useful when applied to real-scale wire-wrapped fuel bundles in the past, when computer resources were not powerful. However, subchannel analysis codes cannot predict locally developed vortical and separated flow phenomena, factors that have significant effects on the secondary flow in a subchannel.

There has been an enormous growth in the computing capability over the past 70 years since the introduction of the electronic numerical integrator and computer. In the past, computational fluid dynamics (CFD) analysis of full-scale fuel assembly could not be implemented because of the computing capability. Recently, a huge increase in computer power allows three-dimensional simulation of the thermal hydraulics of wire-wrapped fuel bundles. Ahmad et al. [12], Gajapathy et al. [13], and Péniguel et al. [14] performed a three-dimensional flow and heat transfer analysis using a Reynolds-averaged Navier–Stokes (RANS)-based simulation. Raza and Kim [15] investigated three kinds of cross-sectional shapes of wire spacers (circle, hexagon, and rhombus) using the RANS-based simulation. The overall pressure drop was highest in the case of rhombus-shaped wire spacers. Fischer et al. [16] carried out a large eddy simulation (LES) for investigation of flow around a wire-wrapped fuel pin.

In this study, three-dimensional flow phenomena in a wire-wrapped 37-pin fuel assembly mock-up of a Japanese loop-type SFR Monju were investigated by a numerical analysis using the general-purpose commercial CFD code CFX. Complicated and vortical flow phenomena in the wire-wrapped 37-pin fuel assembly were captured by a RANS flow simulation using a shear stress transport (SST) turbulence model, and by the vortex structure identification technique based on the critical point theory [17]. The RANS-based flow simulation without any trimmed shape between pin surface and wire surface was carried out in this study.

2. Test section

The experimental test of the wire-wrapped 37-pin fuel bundle [18] was conducted at JNC's Oarai Engineering Center. Design specifications of the 37-pin fuel assembly are summarized in Table 1. The fuel bundle, the pitch-to-diameter ratio of which is 1.14, was centered in a hexagonal tube, with a 60.94 mm flat-to-flat distance inside. A total of 37 pins (8.5 mm in diameter) were wrapped by wire spacers (1.1 mm in diameter) with a wrapping lead of 200 mm. The fuel rods have an electrically heated length of 650 mm. Fig. 1 shows a schematic of the test section of the 37-pin fuel assembly. As shown in Fig. 1, the electrically heated section of the 37-pin bundle is located at 500 mm downstream of the fuel assembly inlet domain.

3. Numerical analysis method

3.1. *Test section of numerical analysis*

Fig. 2 shows the test section of numerical analysis of pressure distribution on the duct wall surface of the heated location of the hexagonal duct. As shown in Fig. 1 and 2, the present CFD investigation was carried out over the full-scale experimental facility of SIENA's 37-pin fuel assembly. Pressure distribution on the duct wall surface of the heated test section has a helically periodic pattern, which has the same length as the wire spacer lead pitch. In the present study, the RANS simulation using the SST turbulence model, for investigating the three-dimensional and vortical flow phenomena, was conducted with a high-resolution scheme. Convergence of the simulation was judged by the periodic temperature variations in the outlet domain of the 37-pin fuel assembly.

Table 1 – Geometric parameters of test section.

Geometric parameters	Values
Number of pins	37
Pin diameter	8.5
Pin pitch	9.65
Pin axial length	1650
Heated length	650
Heat flux distribution	Uniform
Tube flat-to-flat distance	60.94
Wire spacer diameter	1.1
Wire lead pitch	200

Data are presented as mm unless otherwise indicated.

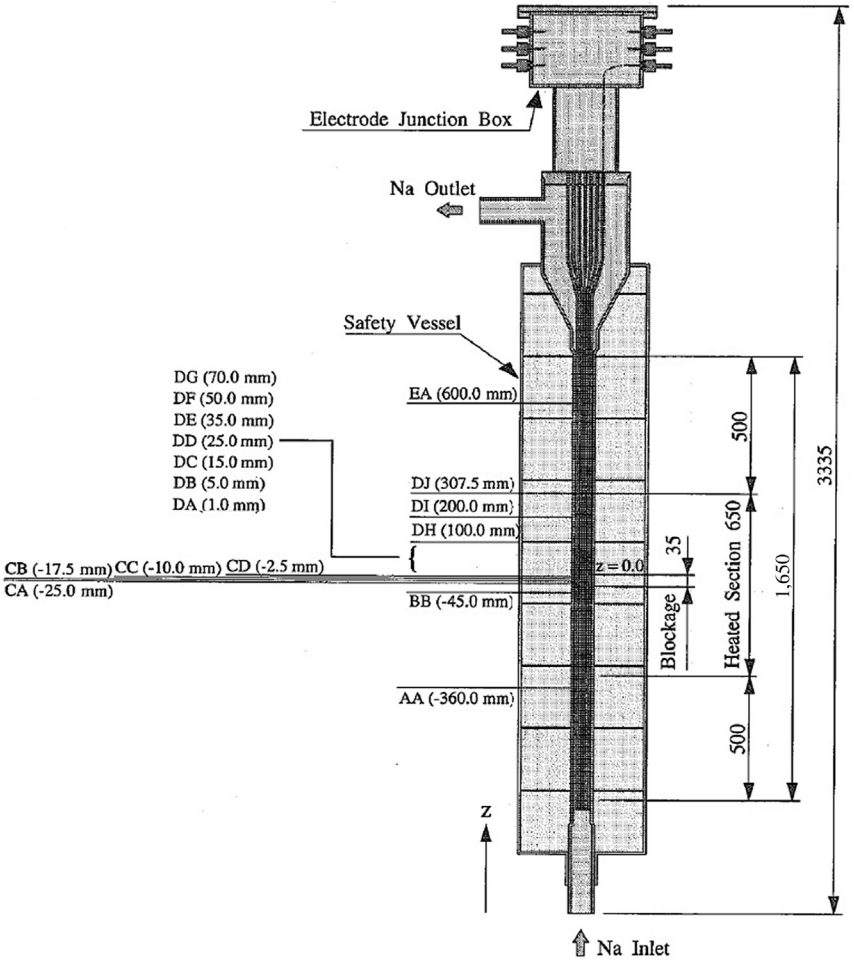

Fig. 1 – Schematic of the test section [18].

3.2. *Computational grids and boundary conditions*

The computational grid system of the 37-pin fuel assembly is composed of hexahedral meshes. Fig. 3 shows the perspective view of the CFD analysis. As shown in Fig. 3, all fuel bundles are numbered from 1 to 37 in clockwise and radial directions. Fuel bundle geometries, such as diameters of the rods and wires, were fully simulated in this study. Table 2 describes the computational grid system. As shown in Table 2, the computational grid system is divided into two regions, the fluid part and the structure part, using the in-house code of mesh generation. The total number of computational grids in the system is approximately 9.89×10^6 cells. Table 3 describes the computational boundary condition of the CFD analysis in the test assembly. As shown in Table 3, the inlet and outlet are defined with a constant velocity of various values and a relative pressure of 0 Pa, respectively. The rod outer and wire outer are defined with a no slip condition and smooth roughness. A duct wall is applied to the no slip and adiabatic conditions.

3.3. *Turbulence model*

Numerical simulation techniques of a turbulent flow are typically divided into direct numerical simulation (DNS), LES, and RANS simulation. DNS resolves the whole range of spatial and temporal scales of the turbulence. As the grid and time scales of DNS need to be less than the Kolmogorov scale, which is the smallest dissipative scale, the DNS requires fine grids and a small time interval. LES solves spatially filtered Navier–Stokes equations on coarser grids. Thus, the LES does not resolve the entire scale of turbulent flows, but resolves only large scales of a turbulent flow. Small scales of turbulent flow are modeled using subgrid scale models developed by Smagorinsky [19]. RANS simulation solves the time-averaged Navier–Stokes equations and models all scales of turbulence using turbulence models such as k–ε, k–w, and SST.

Assuming that computing cost of the RANS simulation is equal to 1, costs of the DNS and LES increase as the cube and square of the Reynolds number, respectively. The Reynolds number, based on the averaged axial velocity and the hydraulic diameter of the present fuel assembly, is higher than 4.29×10^4. For this reason, DNS and LES are not feasible methods for the 37-pin fuel assembly. RANS simulation is a very practical and affordable engineering solution with good knowledge of turbulence.

Turbulence models for the RANS equations are used for computing the Reynolds stress tensor from turbulent fluctuations in the fluid momentum. Turbulence models such as

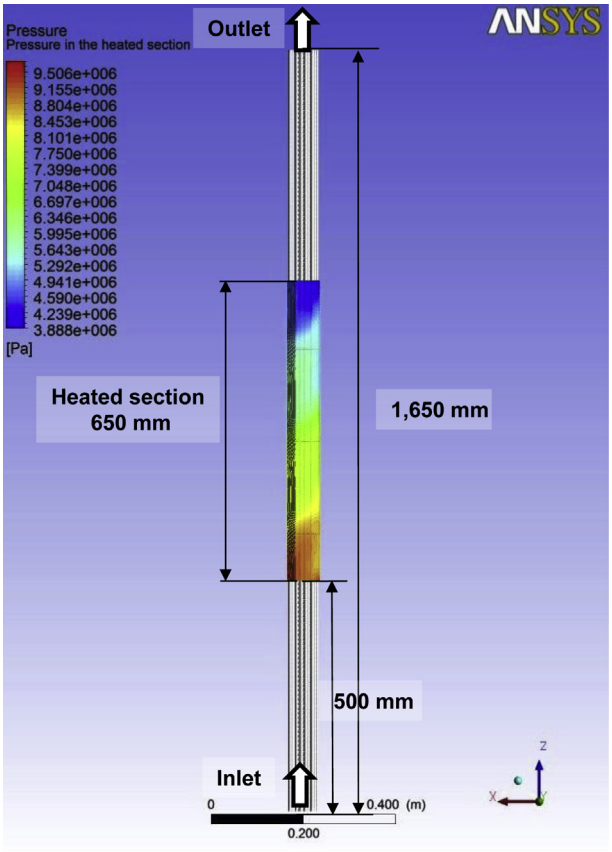

Fig. 2 – Test section with pressure distribution on the duct wall surface of the heated position.

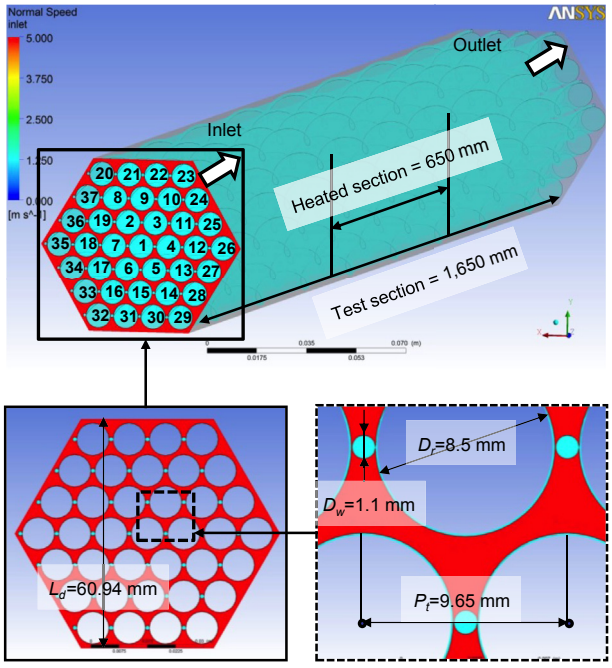

Fig. 3 – Perspective view of the CFD analysis. CFD, computational fluid dynamics.

Table 2 – Computational grids system.

Grid region	Cells	Nodes	Elements
Subchannels	7,510,800	8,943,016	7,510,800
Cladding	1,862,025	2,142,266	1,862,025
Wire	512,820	590,001	512,820
Total	9,885,645	11,675,283	9,885,645

$k-\varepsilon$, $k-w$, and SST have become industry standard models and are commonly used for most types of engineering problems, although the $k-\varepsilon$ model shows weakness in cases of large adverse pressure gradients, and the $k-w$ model is too sensitive to the inlet free-stream turbulence properties [20]. The SST model can overcome the above problems by switching to the $k-\varepsilon$ model in the free stream and to the $k-w$ model in the viscous sublayer [21]. The minimum grid scale on the fuel rod surface was 5.0×10^{-7} mm. This was to capture the transition from a laminar to a turbulent flow with the SST turbulence model. The friction velocity y^+ is close to 1.

Sensitivity studies of turbulence models, such as $k-\varepsilon$, $k-w$, and SST, were implemented. Fig. 4 shows the friction factors of different turbulence models in the wire-wrapped 37-pin fuel assembly. As shown in Fig. 4, friction factors of the $k-w$ model are 2.8–5.8% higher than that with the $k-\varepsilon$ model. The friction factor seen with the SST model is 1.4–1.6% smaller than that of the $k-w$ model. Since the SST model switches to the $k-\varepsilon$ and $k-w$ models, the value of the friction factor of the SST model is between the values of the $k-\varepsilon$ and $k-w$ models.

3.4. *Grid dependency test of friction factor*

The CFD analysis results of the SST turbulence model are dependent on the grid scale. Fig. 5 shows the friction factors with different wall-normal and stream-wise grid spacing in the wire-wrapped 37-pin fuel assembly. Evaluated wall-normal grid-spacing scales, y+, are 1.0, 2.5, and 10.0. As shown in Fig. 5A, uncertainties of friction factors with different wall grid spacing in the CFD simulation with the SST turbulence model were under 1.6%. Friction factors with different stream-wise grid lengths normalized by the rod diameter are shown in Fig. 5B. As shown in Fig. 5B, the maximum friction factor differences are 7.8–11.1%. Based on the grid sensitivity study, the wall-normal grid spacing is more sensitive to the CFD analysis results than the stream-wise grid spacing.

Table 3 – Boundary condition of CFD analysis.

Boundary domain	Condition	Value
Inlet	Constant velocity	Various
Outlet	Relative pressure	0 (Pa)
Rod outer	No slip	–
Wire outer	Smooth wall	
Duct wall	No slip (adiabatic)	–

CFD, computational fluid dynamics.

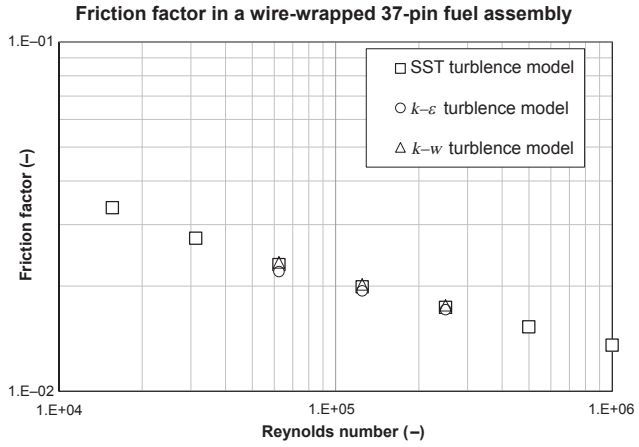

Fig. 4 – Friction factors of different turbulence models in the wire-wrapped 37-pin fuel assembly. SST, shear stress transport.

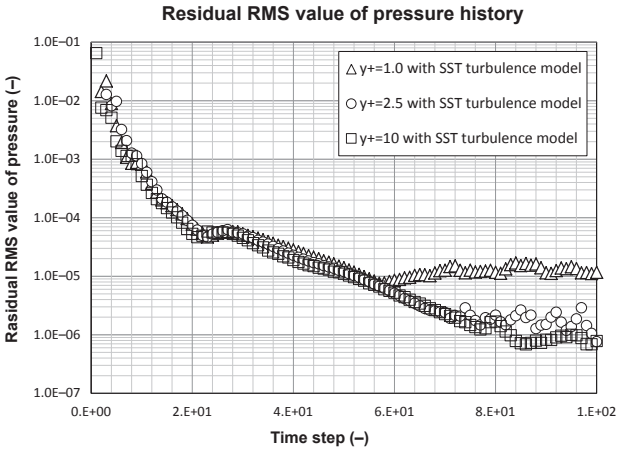

Fig. 6 – Maximum residual RMS value time history of pressure in the wire-wrapped 37-pin fuel assembly. RMS, root mean square; SST, shear stress transport.

Fig. 6 shows the maximum residual root mean square value time history of pressure over the computational grid system. As shown in Fig. 6, the maximum residual root mean square value of pressure with time is not significantly dependent on the wall grid spacing. In this study of the wire-wrapped 37-pin fuel assembly, the CFD simulation results with the wall y^+ grid scale of 1 has been analyzed to capture the details of complicated and vortical flow structures in the boundary layer.

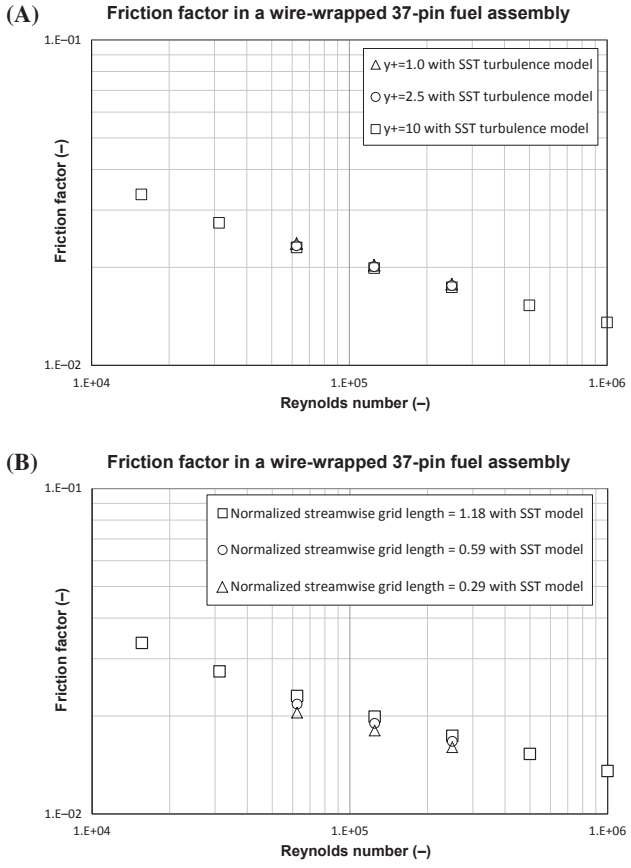

Fig. 5 – Friction factors with different grid length scales in the wire-wrapped 37-pin fuel assembly. (A) Different wall-normal grid spacing. (B) Different stream-wise grid spacing. SST, shear stress transport.

4. Analysis results

4.1. *Test section of numerical analysis*

4.1.1. *Pressure drop correlations*

Friction factor correlations, such as the Rehme [2] model, Engel et al. [3] model, and Cheng and Todreas [4] simplified model, are widely used for a wire-wrapped fuel bundle. Each friction factor is calculated using the following correlations. All the various symbols have been defined in the Nomenclature section of this paper. The Rehme [2] model, Engel et al. [3] model, and Cheng and Todreas [4] simplified model can be defined by Eqs. (1)–(3):

$$f = \left(\frac{64}{\mathrm{Re}}\cdot F^{0.5} + \frac{0.0816}{\mathrm{Re}^{0.1333}}\right)\cdot\frac{N_r\cdot\pi\cdot(D_r+D_w)}{S_t} \tag{1}$$

$$\text{Where: } F = \left(\frac{P_t}{D_r}\right)^{0.5} + \left[7.6\cdot\frac{(D_r+D_w)}{H}\cdot\left(\frac{P_t}{D_r}\right)^2\right]$$

$$\text{Laminar flow}: f = \frac{110}{\mathrm{Re}} \text{ for } \mathrm{Re}\le 400,$$

$$\text{Turbulent flow}: f = \frac{0.55}{\mathrm{Re}^{0.25}} \text{ for } \mathrm{Re}\ge 5000,$$

$$\text{Transition flow}: f = \frac{110}{\mathrm{Re}}\cdot(1-\psi)^{0.5} + \frac{0.55}{\mathrm{Re}^{0.25}}\cdot\psi^{0.5} \text{ for } 400\le \mathrm{Re}\le 5000 \tag{2}$$

$$\text{Where: } \psi = \frac{(\mathrm{Re}-400)}{4600\,\mathrm{Re}}$$

$$\text{Laminar flow}: f=\frac{C_{fL}}{\mathrm{Re}} \text{ for } \mathrm{Re}\le \mathrm{Re}_L,$$

$$\text{Turbulent flow}: f=\frac{C_{fT}}{\mathrm{Re}^{0.18}} \text{ for } \mathrm{Re}_T\le \mathrm{Re},$$

$$\text{Transition flow}: f=\frac{C_{fL}}{\mathrm{Re}}\cdot(1-\psi)^{1/3}+\frac{C_{fT}}{\mathrm{Re}^{0.18}}\cdot\psi^{1/3} \text{ for } \mathrm{Re}_L\le \mathrm{Re}\le \mathrm{Re}_T \quad (3)$$

Where:

$$\log\left(\frac{\mathrm{Re}_L}{300}\right)=1.7\cdot\left(\frac{P_t}{D_r}-1.0\right),$$

$$\log\left(\frac{\mathrm{Re}_T}{10000}\right)=0.7\cdot\left(\frac{P_t}{D_r}-1.0\right),$$

$$\psi=\left(\log(\mathrm{Re})-\left(1.7\cdot\frac{P_t}{D_r}+0.78\right)\right)\Big/\left(2.52-\frac{P_t}{D_r}\right)$$

$$C_{fL}=\left(-974.6+1612.0\cdot\left(\frac{P_t}{D_r}\right)-598.5\cdot\left(\frac{P_t}{D_r}\right)^2\right)\cdot\left(\frac{H}{D_r+D_w}\right)^{0.06-0.085\cdot(P_t/D_r)}$$

$$C_{fT}=\left(\begin{array}{l}0.8063-0.9022\cdot\log\left(\frac{H}{D_r+D_w}\right)\\ \\ +0.3526\cdot\left(\log\left(\frac{H}{D_r+D_w}\right)\right)^2\end{array}\right)\cdot\left(\frac{P_t}{D_r}\right)^{9.7}\cdot\left(\frac{H}{D_r+D_w}\right)^{1.78-2\cdot(P_t/D_r)}$$

4.1.2. *Comparison of CFD with pressure drop correlations*

Fig. 7 shows a comparison of the CFD analysis results with the friction factor correlations of the Rehme [2] model, Engel et al. [3] model, and Cheng and Todreas [4] simplified model in various Reynolds number ranges. Based on the engineering judgment of Bubelis and Schikorr [22], friction factor correlations provide a generally good fit with all the various experimental data sets for different wire-wrapped bundle configurations such as pin diameter, pin pitch, and wire lead pitch. In case of the wire-wrapped 37-pin fuel assembly mock-up, the CFD analysis results agree rather well with the Cheng and Todreas [4] model. Fig. 8 shows the axially distributed friction factors. As shown in Fig. 8, friction factors of the inlet region are also overestimated until the inlet flow reaches the end position of the second periodical wire lead pitch.

4.2. *Three-dimensional flow field*

A three-dimensional flow field at a Reynolds number of 5.0×10^5 is investigated in this chapter. Fig. 9 shows the pressure distribution with local contours and projected streamlines on the cross-sectional planes, which are perpendicular to the axial direction and are viewed from the inlet. Fig. 9A–C show the CFD analysis results for 850 mm, 900 mm, and 950 mm, respectively. As shown in Fig. 9A–C, large-scale vortex structures between the hexagonal duct wall and the wire-wrapped bundle are developed in the clockwise direction along the axial direction. As the wires are helically wrapped along the axial direction, they have a relative position with respect to the stationary hexagonal duct wall. The relative position will be closely related to the behavior of the vortex structure and three-dimensional flow phenomena.

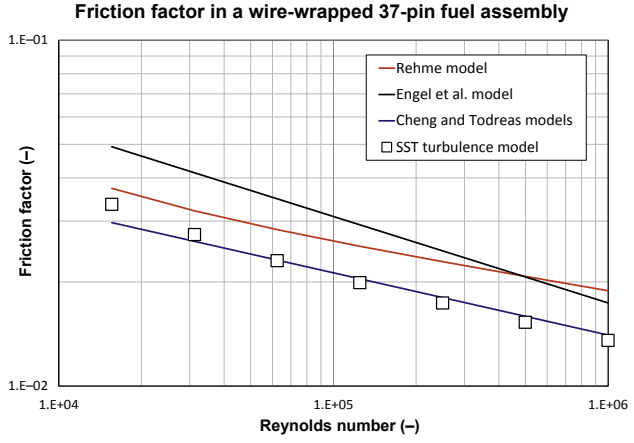

Fig. 7 – Comparison of the CFD analysis results with friction factor correlations in the wire-wrapped 37-pin fuel assembly. CFD, computational fluid dynamics; SST, shear stress transport.

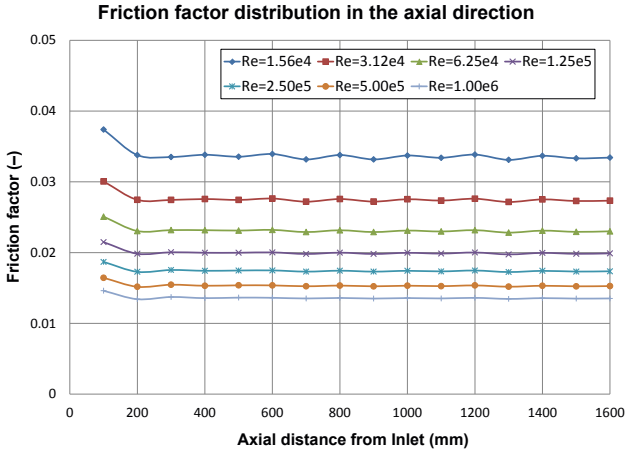

Fig. 8 – Stream-wise friction factor distribution in the wire-wrapped 37-pin fuel assembly.

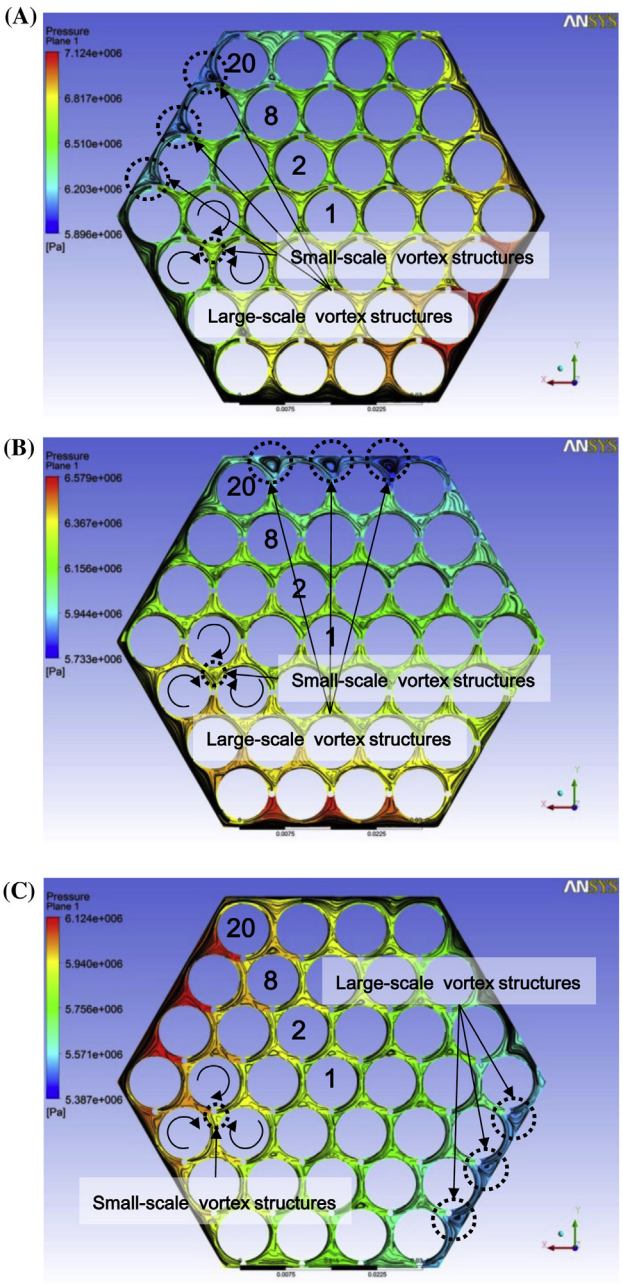

Fig. 9 – Pressure distribution with local contours and projected streamlines on the cross-sectional planes: (A) 850 mm axial position from the inlet; (B) 900 mm axial position from the inlet; and (C) 950 mm axial position from the inlet.

Fig. 10 shows the projected streamlines on the cross-sectional planes of 850 mm, 875 mm, 900 mm, 925 mm, and 950 mm, which correspond to the relative position of the wire of 90°, 135°, 180°, 225°, and 270°, respectively. As shown in Fig. 10, multiscale vortex structures are developed in the fuel assembly. The vortical and separated flow fields are composed of corner vortex structures (yellow dotted lines) in the corner subchannels, edge vortex structures (white dotted lines) in the edge subchannels, and interior vortex structures (red dotted lines) in the interior vortex subchannels. The location of the

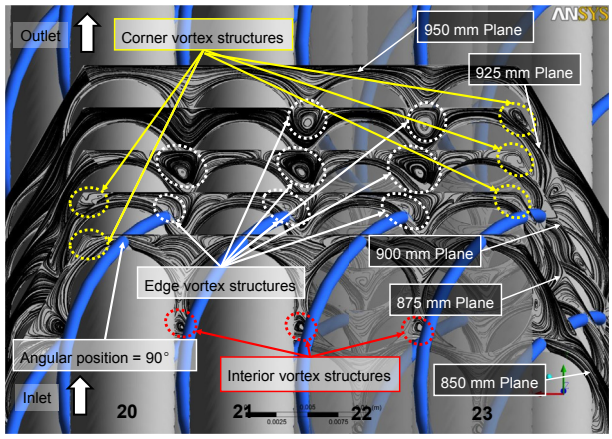

Fig. 10 – Projected streamlines on the cross-sectional planes of 850 mm, 875 mm, 900 mm, 925 mm, and 950 mm.

corner and edge vortex structures is closely related to the relative position between the wire and the duct wall. As shown in Fig. 10, the corner and edge vortex structures are formed in a tangential direction when their distance from the wire is more than that from the duct wall.

Fig. 11 shows the axial velocity (Z-axis) distribution and projected streamlines on the cross-sectional planes. Regardless of the large-scale vortex structures in the edge subchannels, the edge subchannels have axially higher velocity than corner and interior subchannels, as shown in Fig. 11. This means that axially acting blockage effects due to vortex structures do not occur in the edge subchannels. However, the corner vortex structures partially induce the axially acting blockage effect. These strong longitudinal vortex structures in the edge subchannels can achieve better heat transfer characteristics than those in the corner and interior sub-channels.

Fig. 12 shows the secondary velocity (X- and Y-axis) distribution and projected streamlines on the cross-sectional planes. Wire spacers induce a secondary flow of up to about

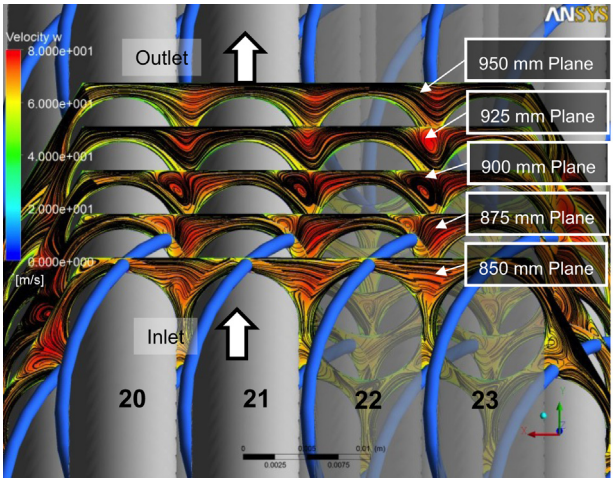

Fig. 11 – Axial velocity (Z-axis) distribution and projected streamlines on the cross-sectional planes.

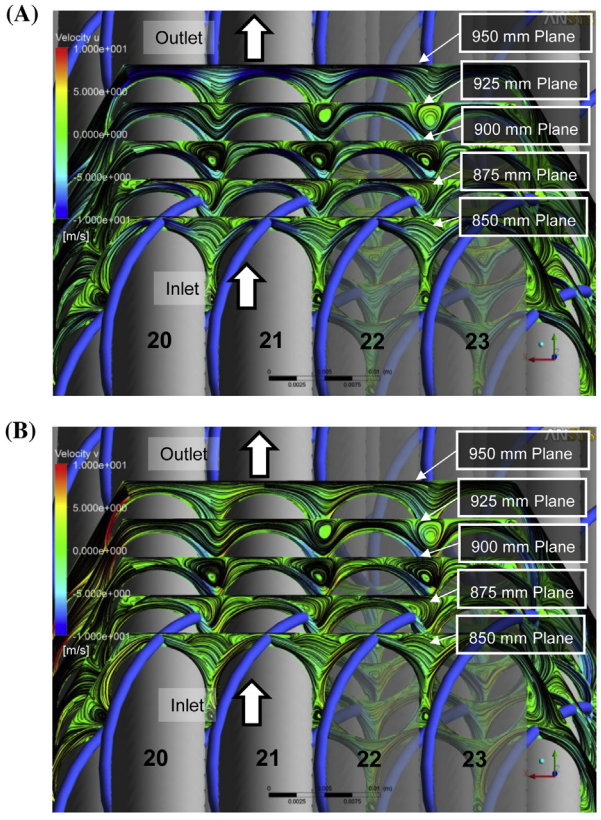

Fig. 12 – Secondary velocity (X- and Y-axis) distribution and projected streamlines on the cross-sectional planes. (A) Velocity distribution in the X-direction. (B) Velocity distribution in the Y-direction.

13% of the magnitude of the axial velocity. The secondary flow in the corner and edge subchannels is much stronger than that in the interior subchannels.

Fig. 13 shows the velocity distribution and projected streamlines on the cross-sectional plane at a height of 800 mm from the inlet domain. To obtain the quantitatively assessed axial velocity, the cross-sectional plane in Fig. 13 is divided into inner, middle, and outer regions using the radius. Table 4 describes the area-averaged velocity normalized by the magnitude of the inlet mean velocity on the inner, middle, and outer subchannels. The axial velocity averaged in the outer regions is about 13% higher than that averaged in the middle and inner sub-channels.

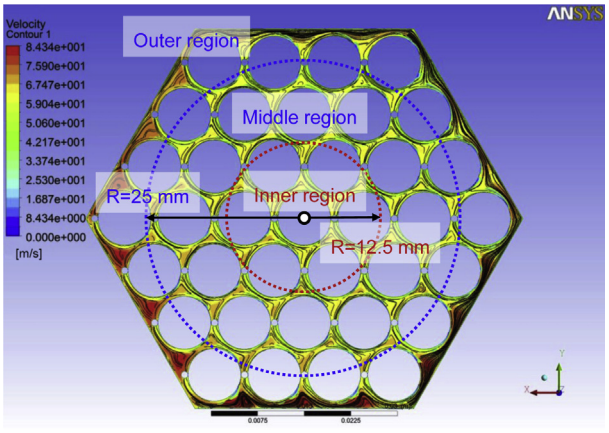

Fig. 13 – Velocity distribution and projected streamlines on the cross-sectional plane at a height of 800 mm from the inlet domain.

4.3. *Effect of wire spacers*

Behavior of the secondary flow in the edge, corner, and interior subchannels is investigated by an assessment of the driving force, calculated from the pressure on the wire wall surface. An analysis of the wire effect in the fuel assembly was conducted at a Reynolds number of 5.0×10^5. Fig. 14 shows the pressure distribution and limiting streamlines on the wire surface. Fig. 14A and 14B show the pressure surface and suction surface, respectively. As shown in Fig. 14A, the attachment line due to stagnation of flow is induced at the center of the pressure surface. In Fig. 14B, the separation line is formed at the center of the suction surface. The separation position of the suction surface dominates the behavior of a small-scale vortex located near the interface part between the rod and the wire.

The driving force on the wire surfaces is normalized by the dynamic pressure of the inlet region. Fig. 15 shows a schematic of the driving force on the wire wall surface of 25 mm axial length. As shown in Fig. 12, the driving forces of the secondary flow are the forces in the X- and Y-direction. The drag force against the axial direction is the Z-direction. The driving forces on the wire surface of 25 mm are defined as follows:

$$F_{n,25mm} = \frac{F_{25mm}}{(0.5\cdot\rho\cdot v^2)\cdot(D_w\cdot(\pi\cdot D_r)/N)} \tag{4}$$

All the symbols used here are defined in the Nomenclature section of this paper.

Fig. 16 shows the normalized driving force on the wire surface of 25 mm with different angular positions and rod locations. The angular position on the cross-sectional coordinate (X- and Y-axis) is defined as follows:

$$A = \tan^{-1}\frac{(Y_{\text{center of wire}} - Y_{\text{center of rod}})}{(X_{\text{center of wire}} - X_{\text{center of rod}})} \tag{5}$$

All the symbols used here are defined in the Nomenclature section of this paper.

Fig. 16A–C describe the driving forces in the X-, Y-, and Z-direction, respectively. As shown in Fig. 16, the effects of the

Table 4 – Area-averaged velocity in the inner, middle, and outer regions.

Parameters	Inner region (R < 12.5 mm)	Middle region (12.5 mm < R < 25 mm)	Outer region (R > 25 mm)
X-velocity	0.0240	0.0207	0.0022
Y-velocity	0.0337	0.0298	−0.0030
Z-velocity	0.9578	0.9550	1.0785

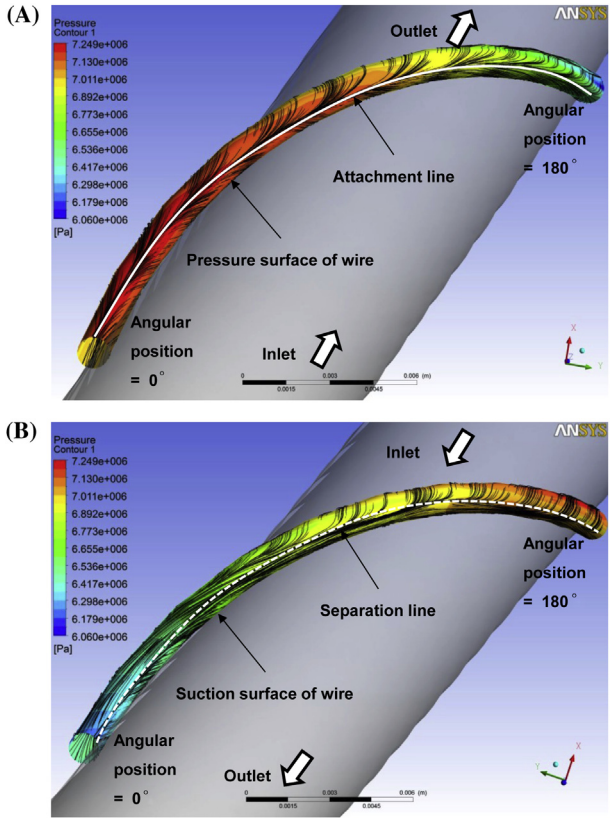

Fig. 14 – Pressure distribution and limiting streamlines on the wire wall surface. (A) Wire pressure surface from upstream view. (B) Wire suction surface from downstream view.

driving forces on the wire are significantly dependent on the angular position of the wire and the rod position in the duct. The driving force in the X-direction of rod number 20 is 263% higher than that of rod number 1 at an angular position of 67.5°. The driving force in the Y-direction of rod number 20 is

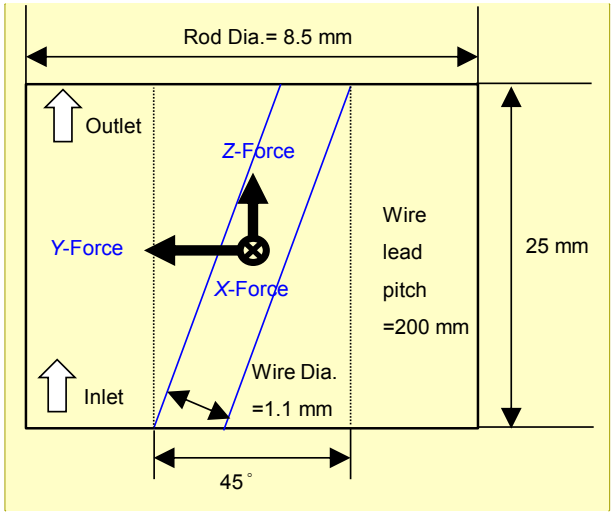

Fig. 15 – Schematic of the driving forces on the wire wall surface of 25 mm axial length.

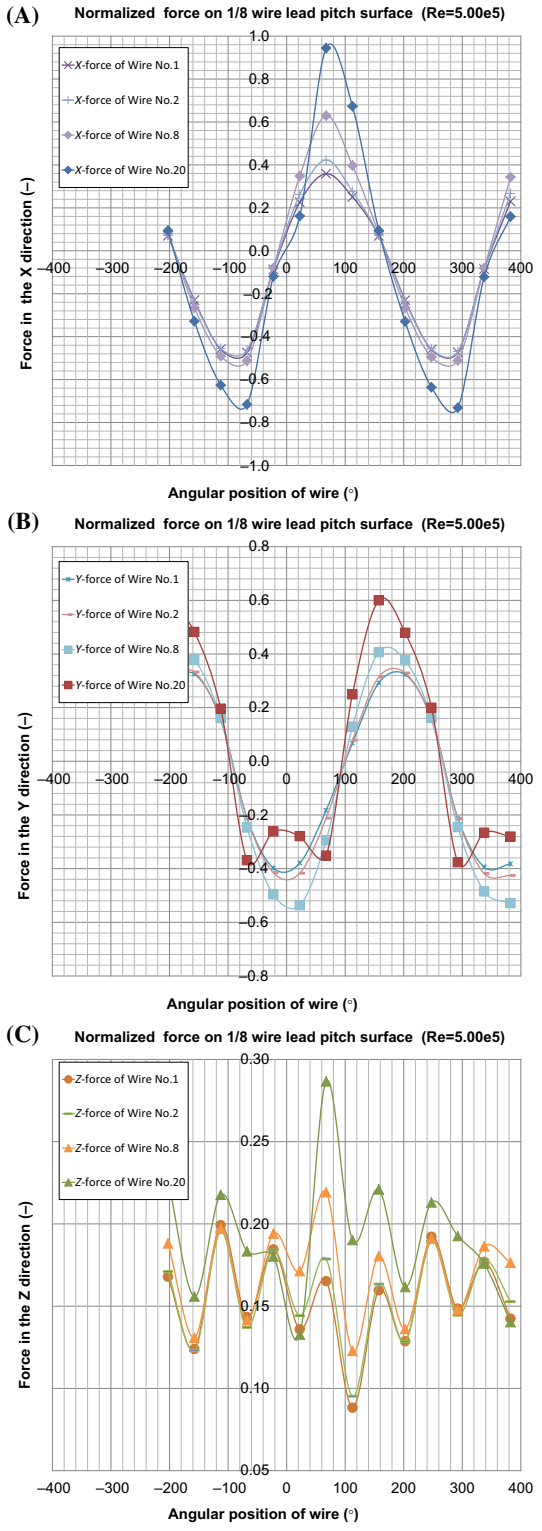

Fig. 16 – Normalized driving forces on the wire wall surface of 25 mm on each difference rod position over wire angular position. (A) Driving force in the X-direction. (B) Driving force in the Y-direction. (C) Driving force in the Z-direction.

205% higher than that of rod number 1 at an angular position of 157.5°. The driving force in the Y-direction of rod number 20 is 174% higher than that of rod number 1 at an angular position of 67.5°. The driving force in the Z-direction increases as the square of the velocity in a subchannel [23]. However, driving forces in the X- and Y-direction are not only dependent on the axial velocity, but also significantly dependent on the relative angular position between the wire and the duct wall. Based on the investigation results of the driving force on the wire, it is strongly recommended that the duct wall effect caused by the relative position between the wire and the duct should be considered.

5. Discussion

Three-dimensional flow phenomena in a wire-wrapped 37-pin fuel assembly have been investigated by a numerical analysis using a general-purpose commercial CFD code, CFX. Complicated and vortical flow phenomena in the wire-wrapped 37-pin fuel assembly were elucidated by the RANS flow simulation using the SST turbulence model. The major conclusions of the study are as follows.

The secondary flow in corner and edge subchannels is much stronger than that in interior subchannels. Wire spacers induce a secondary flow of up to about 13% of the magnitude of the axial inlet velocity. The axial velocity averaged in the corner and edge subchannels is about 13% higher than that averaged in the interior subchannels.

Three-dimensional multiscale vortex structures start to be formed by the interaction between the secondary flows around each wire-wrapped pin. Large-scale and small-scale vortex structures are generated in the corner and edge subchannels, and the inner subchannels, respectively. Behavior of the large-scale vortex in the corner and edge subchannels is closely related to the relative position between the hexagonal duct wall and the wire spacer. Regardless of the relative position between the adjacent rod and the wire spacer, the small-scale vortex is axially developed in the interior subchannels.

The effects of the driving forces on the wire are remarkably dependent on the angular position of the wire and the rod position in the hexagonal duct. Driving forces caused by the wire spacer in the X-, Y-, and Z-direction of rod number 20 are 263%, 205%, and 174% higher than those of rod number 1 at angular positions of 67.5°, 157.5°, and 67.5°, respectively at certain analyzed Reynolds number.

Conflicts of interest

The authors declare no conflict of interest.

Acknowledgments

This study was supported by the Ministry of Science, ICT, and Future Planning of Korea. This work was supported by the National Research Foundation of Korea (NRF) grant funded by the Korean government MSIP (No. 2012M2A8A2025634).

Nomenclature

A	Angular position of wire spacer defined in Eq. (5) (degree)
C_f	Friction factor constant defined in Eq. (3) (unitless)
D_r	Rod diameter (m)
D_w	Wire diameter (m)
F	Friction factor (unitless)
F_{25mm}	Force acted on a wire of 25 mm (N)
$F_{n,25mm}$	Normalized F_{25mm} (N)
H	Wire spacer lead pitch (m)
N	Number of fuel pins (unitless)
N_r	Number of fuel pins (unitless)
P_t	Rod pitch for wire-wrap configuration (m), $= D_r + 1.044 \times D_w$
Re	Reynolds number (unitless)
S_t	Total wetted perimeter (m)
V	Inlet velocity (m/s)
X	X coordinate (m)
Y	Y coordinate (m)
ρ	Sodium density (kg/m^3)
Ψ	Intermittency factor (unitless)

Subscripts

F	Denotes friction factor
l, L	Denotes laminar flow region
t, T	Denotes turbulent flow region

REFERENCES

[1] E.H. Novendstern, Turbulent flow pressure drop model for fuel rod assemblies utilizing a helical wire-wrap spacer system, Nucl. Eng. Des. 22 (1972) 19–27.
[2] K. Rehme, Pressure drop correlations for fuel element spacers, Nucl. Technol. 17 (1973) 15–23.
[3] F.C. Engel, R.A. Markley, A.A. Bishop, Laminar, transition and turbulent parallel flow pressure drop across wire-wrap-spaced rod bundles, Nucl. Sci. Eng. 69 (1979) 290–296.
[4] S.K. Cheng, N.E. Todreas, Hydrodynamic models and correlations for bare and wire-wrapped hexagonal rod bundles—bundle friction factors, sub-channel friction factors and mixing parameters, Nucl. Eng. Des. 92 (1986) 227–251.
[5] R.M. Roidt, L.J. Harper, T.G. Bartholet, Experimental determination of interior subchannel crossflow and axial flow in a model of the Clinch River Breeder Reactor fuel assembly rod bundle with wire wrap spacers, American Society of Mechanical Engineers Paper, 76-WA/HT-83.
[6] M.H. Chun, K.W. Seo, An experimental study and assessment of existing friction factor correlations for wire-wrapped fuel assemblies, Ann. Nucl. Energy 28 (2001) 1683–1695.
[7] S.K. Choi, K. Choi, H.Y. Nam, J.H. Choi, H.K. Choi, Measurement of pressure drop in a full-scale fuel assembly of a liquid metal reactor, J. Pressure Vessel Technol. 125 (2003) 233–238.
[8] D.S. Rowe, COBRA III-C: A Digital Computer Program for Steady State and Transient Thermal Hydraulic Analysis of Nuclear Fuel Elements, Battle Pacific Northwest Laboratories, BNWL-1695, 1973.
[9] J.D. Macdougall, J.N. Lillington, The SABRE code for fuel rod cluster thermo-hydraulics, Nucl. Eng. Des. 82 (1984) 171–190.

[10] H. Ninokata, ASFRE-III: A Computer Program for Triangular Rod Array Thermo-hydraulic Analysis of Fast Breeder Reactors, PNC Report, PNC N941 85-106, 1985.
[11] W.S. Kim, Y.G. Kim, Y.J. Kim, A subchannel analysis code MATRA-LMR for wire wrapped LMR subassembly, Ann. Nucl. Energy 29 (2002) 303–321.
[12] I. Ahmad, K.Y. Kim, Flow and convective heat transfer analysis using RANS for a wire-wrapped fuel assembly, J. Mech. Sci. Technol. 20 (2006) 1514–1524.
[13] R. Gajapathy, K. Velusamy, P. Selvaraj, P. Chellapandi, S.C. Chetal, CFD investigation of helical wire-wrapped 7-pin fuel bundle and the challenges in modeling full scale 217 pin bundle, Nucl. Eng. Des. 237 (2007) 2332–2342.
[14] C. Péniguel, I. Rupp, J. Juhel, M. Guillaud, N. Gervais, S. Rolfo, Three dimensional conjugated heat transfer analysis in sodium fast reactor wire-wrapped fuel assembly, in: Proceedings of ICAPP '09, Paper 9311, Tokyo, Japan, 2009.
[15] W. Raza, K.Y. Kim, Shape optimization of wire-wrapped fuel assembly using Kriging metamodeling technique, Nucl. Eng. Des. 238 (2008) 1332–1341.
[16] P.F. Fischer, A. Siegel, P. Palmiotti, Large eddy simulation of wire wrapped fuel pins I: hydrodynamics in a periodic array, in: Proceedings of M&C + SNA, Monterey, California, 2007.
[17] A.E. Perry, M.S. Chong, A description of eddying motions and flow patterns using critical-point concepts, Annu. Rev. Fluid Mech. 19 (2009) 125–155.
[18] T. Iitsuka, Y. Oki, S. Kawashima, M. Nishimura, T. Isozaki, H. Kamide, Study for subassembly porous blockage in fast breeder reactors—pre-sub-channel analysis of 37-pin bundle sodium test, PNC TN9410 98-022, 1998.
[19] J. Smagorinsky, General circulation experiments with the primitive equations. I. The basic experiment, Monthly Weather Rev. 91 (1963) 99–165.
[20] D.C. Wilcox, Reassessment of the scale-determining equation for advanced turbulence models, AIAA J. 26 (1998) 1299–1310.
[21] F.R. Menter, Two-equation eddy-viscosity turbulence models for engineering applications, AIAA J. 32 (1994) 1598–1605.
[22] H. Bubelis, M. Schikorr, Review and Proposal for Best-Fit of Wire-Wrapped Fuel Bundle Friction Factor and Pressure Drop Predictions Using Various Existing Correlations, Mitglied der Hermann von Helmholtz-Gemeinschaft Deutscher Forschungs-zentren (HGF), 2008.
[23] H. Ninokata, A. Efthimiadis, N.E. Todreas, Distributed resistance modeling of wire-wrapped rod bundles, Nucl. Eng. Des. 104 (1987) 93–102.